Journal of Materials Processing Tech. 317 (2023) 117999

Contents lists available at ScienceDirect

Journal of Materials Processing Tech.

journal homepage: www.elsevier.com/locate/jmatprotec

Study on the non-free plastic shear removal of material and cutting-induced deformation of micron-submicron grooves

Yupeng He [a,b,c], Tianfeng Zhou [a,c,*], A. Senthil Kumar [b,**], Xibin Wang [a,c], Jiwang Yan [d]

[a] School of Mechanical Engineering, Beijing Institute of Technology, Beijing 100081, China
[b] Department of Mechanical Engineering, National University of Singapore, 9 Engineering Drive 1, 117575, Singapore
[c] Beijing Institute of Technology Chongqing Innovation Center, Chongqing 401120, China
[d] Department of Mechanical Engineering, Faculty of Science and Technology, Keio University, Yokohama 223-8522, Japan

ARTICLE INFO

Associate Editor: Stefania Bruschi

Keywords:
Non-free cutting
Material removal model
Chip formation
Micron-submicron groove machining
Cutting-induced deformation

ABSTRACT

The shear interference and chip removal interference between different tool edges during non-free cutting are the main reasons for the deformation of micron-submicron grooves. To our best knowledge, the understanding of the non-free cutting of micron-submicron grooves is still not well established. This paper provides new insight into the material removal mechanism and cutting-induced deformation of micron-submicron grooves in non-free cutting. A novel variable shear angle removal model, revealing the difference of material shear at different positions of the tool edge, is established by infinitesimally segmenting the tool edge after analyzing the shear interference and chip removal interference mechanisms. An equation of the local shear angle enables the mathematical derivation of the topography of the shear surface and chip cross-section in the non-free cutting of micron-submicron grooves. The distribution of shear stress in the shear zone is calculated by establishing the relationship between the shear angle and shear stress based on the unequal division shear zone (UDSZ) theory and Johnson-Cook theory. Furthermore, a mechanics model of micron-submicron groove cutting, revealing the deformation mechanism of the micron-submicron grooves, is established using the differential cutting force method. Finite element simulations and high-speed cutting experiments are conducted to analyze the cutting microstate between the tool and the material and the dynamic deformation of the micron-submicron grooves during non-free cutting. The stress trend of the elastic nodes on the tool edge verifies the mechanics model, and the chip morphology verifies the formation of the shear surface and chips. The degree of non-free cutting is higher at the tool edge infinitesimal segments (TEISs) closer to the tool tip, resulting in a smaller shear angle, which makes the extrusion stress suffered by the groove increases nearly twice from top to bottom. The material flow due to dynamic deformation causes the relative cutting line of the rear-side tool edge to shift forward. The deformation of the micron-submicron grooves is related to the stiffness of the structure.

1. Introduction

Researchers have developed innovative methods to manufacture micron-submicron structures to endow materials with optical (He et al., 2021), electrical, magnetic (Malshe et al., 2013), and biomedical properties (Jiang et al., 2019). As shown by Fang et al. (2019), these innovative methods aim to reduce the size and improve the processing accuracy of these structures to achieve multi-functional surfaces. Zhou et al. (2020) reported that the fabrication of three-dimensional (3D) structures at the submicron scale is a key technology required for developing novel applications. Photolithography, especially the use of electron beam exposure by Kowalik et al. (2005) and Qiao et al. (2016), has enabled the fabrication of micron-submicron structures. However, the complex multi-level etching shown by Zhou et al. (2020) makes this technology unsuitable for fabricating 3D structures. Qiao et al. (2016) have shown that femtosecond laser technology has the advantages of high uniformity and high efficiency for creating micron-submicron structures, but it is challenging to create high-quality 3D micron-submicron structures, such as V shape grooves, pyramid arrays, etc. Ultra-precision cutting technology (UPCT) enables the fabrication of 3D structures by removing material. Zhu et al. (2018a,b) and Zhu et al.

* Correspondence to: Key Laboratory of Fundamental Science for Advanced Machining, School of Mechanical Engineering, Beijing Institute of Technology, No. 5 Zhongguancun South Street, Haidian District, Beijing 100081, China.
** Correspondence to: Department of Mechanical Engineering, National University of Singapore, 9 Engineering Drive 1, Singapore 117576, Singapore.
E-mail addresses: zhoutf@bit.edu.cn (T. Zhou), asenthil@nus.edu.sg (A.S. Kumar).

https://doi.org/10.1016/j.jmatprotec.2023.117999
Received 14 February 2023; Received in revised form 17 April 2023; Accepted 23 April 2023
Available online 25 April 2023

Nomenclature

x, y, z	Cartesian axes for groove machining
B-x_t,y_t,z_t	The cartesian coordinate system of the tool
θ	Nose angle of the tool
H	Nominal depth of cut (DoC)
h	Height of the micron-submicron grooves
F_{1t}, F_{1c}	Main cutting force and thrust of tool edge BA
F_{2t}, F_{2c}	Main cutting force and thrust of tool edge BC
F_{3t}, F_{3c}	Main cutting force and thrust of tool edge CD
φ, φ_{crt}	The shear angle of the tool edge infinitesimal segment (TEISs); the limit shear angle of the TEIS at the tool tip
α	The angle between the shear face and the rake face
$\Delta\varphi$	The difference in the local shear angle between non-free cutting and free cutting
a, b	Constants in the shear angle equations
w	Width of the shear zone
β	Friction angle between chip and rake face
dx	Length of TEIS
V_l	The velocity of the material leaving the shear zone
V_c	Cutting velocity
γ_o	Tool rake angle
$\dot{\varepsilon}$, $\dot{\varepsilon}_m$	The shear strain rate of the shear surface and main shear surface
ε, ε_m	The shear strain of the shear surface and main shear surface
k	Positional parameters of the main shear surface
q	Coordinates of the shear surface in the shear zone
τ, τ_m	Shear stress of the shear surface and the main shear surface
A, B, C, n, m,	$\dot{\varepsilon}_0$,T_r, T_m Parameters of the Johnson-Cook model of the materials
T, T_{mx}	The temperature of the shear surface and the main shear surface
ρ, c, μ	Density, specific heat capacity, Taylor-Quinney coefficient of the material
$dF_{\text{local-1}}$, dF_{1c}, dF_{1t}	Cutting force, main cutting force, and thrust of TEIS on edge BA
$F_{\text{local-1}}$	The total cutting force of tool edge BA
σ	Stress acting on the groove surface by the tool edge BA
t	Contact width of the flank to the material

(2015) demonstrated the generation of complex curvilinear trajectories to create micro and hierarchical structures. As demonstrated by He et al. (2020) and Yew Jin et al. (2021), UPCT is a very promising technology for fabricating micro-nano structures due to its high material removal efficiency, flexible control of the groove configuration, and simple process.

The machining quality including shape accuracy is crucial in UPCT. Unlike free cutting, which utilizes a single tool edge. Xue et al. (2021) demonstrated that micron-submicron groove cutting is non-free cutting and involves at least two tool edges. In non-free cutting, as investigated by Qiao et al. (2018), the chip removal at the tool edge causes interferences, resulting in a change in the cutting performance at the microscopic level, adversely affecting the machining quality and accuracy. Therefore, many scholars investigated non-free cutting. The earliest studies by Shi (2018), and Shi and Wang (1995) used the principle of minimum energy to derive the chip removal vector during interference and the equivalent cutting edge method to determine the removal direction of the chip and the cutting force. In these works, the removed material was regarded as a whole, and the differences in material shear at different positions of the tool edge were ignored. In addition, factors influencing the non-free cutting performance were added to the free orthogonal cutting model in the work of Zhang et al. (2018), and the transient cutting force and micro-cutting characteristics were analyzed. The complex non-free cutting process was simplified in these theoretical studies, and the influence of the chip interference on the removal mechanism at the microscopic level was ignored.

Researchers investigated the characteristics of non-free cutting and the evolution of the machining quality of microstructures. V-groove machining has been extensively studied because of its high application potential (Dong et al., 2019). Fang and Xu (2018) demonstrated that a sharp V-shaped tool used for machining the V-shaped groove has a nanometer-level nose radius in advanced tool manufacturing, providing a basic model for analyzing the interference between the two tool edges during non-free cutting. Yan et al. (2009) found that the material flow interference between the two tool edges resulted in material accumulation and the formation of burrs. The unstable material flow and the cutting force caused by non-free cutting caused corrugated defects on the micro-structured surface. The degree of non-free cutting during the machining of grooves is also related to the tool angle. Li et al. (2013) thought that the degree of material deformation during the evolution of the chip from the non-free to the free state is crucial for determining the machining quality. Increasing the nose angle and using a multi-step cutting approach ensures that the material removal process is closer to free cutting; therefore, the material flow, the formation of burrs, and the degree of deformation on the top of the grooves are minimized. By using the finite element method (FEM), Yan et al. (2009) found that the temperature increase caused by chip removal interference can be reduced by multi-step cutting. In addition, Song et al. (2019) demonstrated that non-free cutting can cause an increase in the cutting force. Since most studies focused on grooves at the micron scale or tens of microns, only burrs formed at the top of the grooves were investigated during non-free cutting (Sun et al., 2018), and the slight deformation of the grooves was ignored (Zhu et al., 2018). With an extremely small size, micron and submicron grooves have low stiffness and low resistance to deformation; thus, the deformation induced by the cutting force cannot be ignored. Geng et al. (2018) and Yan et al. (2015) used ultra-small high-quality tools and atomic force microscopy (AFM) probes to fabricate high-quality submicron structures. However, it's hard to further improve the accuracy of microstructures. The cutting-induced deformation differs for microgrooves with different geometries, indicating that the deformation is related to the structure's stiffness, and Song et al. (2019) reduced the cutting-induced deformation to some extent by planning the process path and reducing the amount of cutting for low stiffness structure in each step. Duong et al. (2013), Duong and Kim (2015), and Tauhiduzzaman et al. (2015) used Merchant's free-cutting theory to evaluate cutting-induced deformation, which however is only suitable for calculating the material removal for large microstructures but not for submicron grooves.

As discussed above, to our best knowledge, the material to be removed was commonly considered as a whole, and most studies on non-free cutting were based on analysis of the experimental result. The theory of the chip removal interference and shear mechanism has not been analyzed in detail. Since there is no accurate material removal model revealing the difference of material shear at the different positions at the tool edge, the evolution of the chip morphology during non-free cutting remains unclear. Furthermore, the size of the investigated microstructures has been relatively large, cutting-induced deformation has been ignored, and mechanics models for micron-submicron groove cutting are lacking. Therefore, this paper aims to fill this gap and provides a theoretical basis and experimental proof by establishing a non-free cutting removal model and analyzing the cutting-induced deformation of micron-submicron grooves.

This paper systematically investigates a novel non-free cutting material removal model and cutting-induced deformation of micron-

submicron V-shaped grooves. To begin with, the tool edges and cutting area are assessed separately to determine the mechanisms of shear interference and chip removal interference. A novel variable shear angle removal model, revealing the difference of material shear at different positions of the tool edges, is established by infinitesimally segmenting the tool edge. An equation for the local shear angle is developed, which enables the mathematical derivation of the topography of the shear surface and chip cross-section in the non-free cutting of micron-submicron grooves. Then, the distribution of shear stress in the shear zone is revealed by establishing the relationship between the shear angle and shear stress based on the unequal division shear zone (UDSZ) theory and Johnson-Cook theory. Furthermore, a mechanics model of micron-submicron groove cutting, revealing the deformation mechanism of the micron-submicron grooves, is established using the differential cutting force method. Finally, FEM simulations and high-speed cutting experiments are conducted to analyze the cutting microstate between the tool and the material to determine the dynamic deformation during micron-submicron groove non-free cutting. The mechanics model derived from the variable shear angle model is verified by the stress trend of the elastic nodes on the tool edge, and the shear surface and chip formation theories are verified by the chip topography.

2. Non-free cutting and cutting-induced deformation of micron-submicron grooves

2.1. Generation and deformation of micron-submicron grooves

Since the size of the tool cannot be infinitely small, micron-submicron V-shaped grooves are formed by the residue marks after the material has been removed by the shaping tool during non-free cutting. As shown in Fig. 1a, V-shaped grooves are formed after the material has been removed by the V-shaped tool. The cutting trajectories are parallel. A triangular prism is formed between two adjacent trajectories. The lateral feed rate between the adjacent trajectories and the tool shape determines the size and topography of the groove. However, the tool extrudes material from the target micron-submicron groove, causing deformation, especially on the rear-side tool edge acting on the inclined surface of the triangular prism. Due to the low stiffness, a triangular prism structure is deformed, causing the displacement of the side of the V-shaped groove, as shown in Fig. 1b. When the groove is deformed backward, the dynamic deformation causes a forward shift in the relative cutting line of the rear-side tool edge. As a result, some of the material to be cut is pushed to the back by the rear-side tool edge, creating a residue. The resulting groove has positional and shape errors; these deformation-induced errors are non-negligible and must be prevented.

Non-free cutting exacerbates the degree of deformation. In free cutting, the sheared material moves perpendicularly to the tool edge, and friction and extrusion occur only in the third deformation zone between the sheared material and the rake face during chip removal. In non-free cutting (Fig. 1b), the material is simultaneously sheared by the tool edges on both sides in different directions, causing material flow blockage and chip removal interference. The chip removal interference changes the cutting microstate. Thus, the force on the rear-side tool edge is increased, exacerbating the deformation of the micron-submicron grooves. Moreover, due to a change in the distance between the tool edges on both sides, the interference degree of chip removal is inconsistent, and the cutting microstate changes along the tool edge. When the deformation of the micron-submicron grooves is extensive, the relative shift of the cutting line of the rear-side tool edge in the material increases, resulting in more material residue. Fig. 2 shows a comparison of the material residue on the top of V-shaped grooves for different deformation degrees, which have a period of 380 nm and are created on nickel-phosphorus (Ni-P) material with depth-of-cut (DoC) of 2000 nm and 5000 nm, respectively. The grooves shown in Fig. 2b have higher deformation and more residue. The deformation of the micron-submicron grooves during non-free cutting and the caused material residue are inevitable. Therefore, the establishment of a non-free cutting material removal model and the investigation of the deformation mechanism of the micron-submicron grooves are required.

2.2. Material removal model with variable shear angles in non-free cutting

Deformation and material flow only occur in the plastic domain of the material. The Ni-P material used in this study is plastic during micron-submicron scale cutting. The actual DoC is always much larger than the height of the target micron-submicron grooves, such as H (actual DoC) and h (height of the micron-submicron grooves) due to tool-setting errors and the nominal DoC in micron-submicron groove cutting. The cross-section of the cutting area is asymmetrical, and the tool edges have different lengths on the front and rear sides of the tool. We consider only the main factors to determine the non-free cutting mechanism and therefore material shearing is mainly dominated by the nearest tool edge. The tool edge involved in cutting is divided into three segments (BA, BC, CD) (Fig. 3b), and the cutting area is also divided into three parts since the chip flow occurs perpendicularly to the tool edge

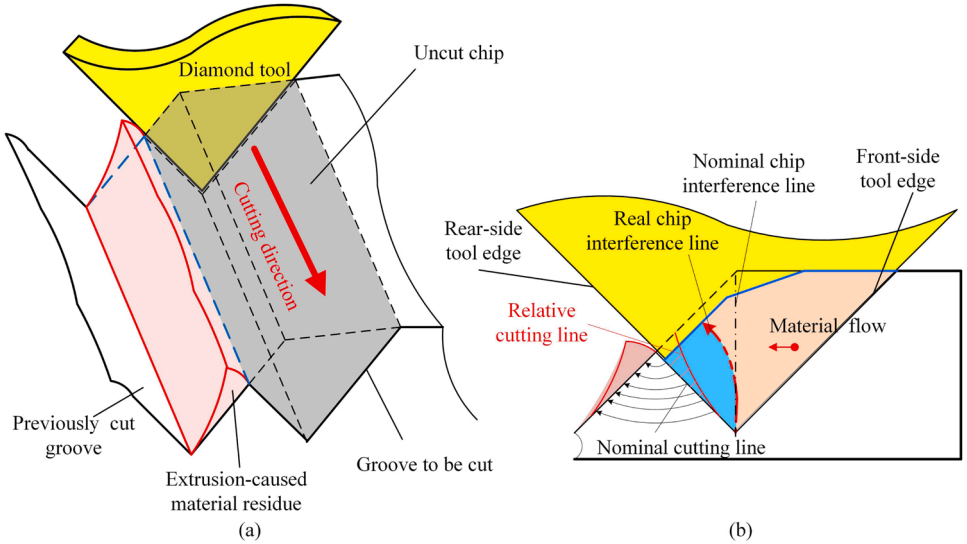

Fig. 1. (a) Illustration of the generation and cutting-induced deformation of micron-submicron grooves. (b) Schematic of the mechanism of extrusion deformation.

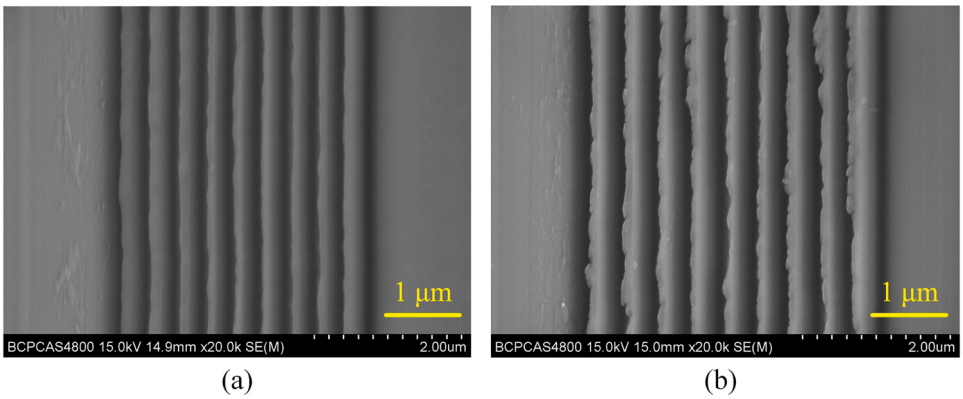

Fig. 2. Comparison of the material residue for different deformation degrees. Grooves with a period of 380 nm are created on Ni-P with DoC of (a) 2000 nm and (b) 5000 nm, respectively.

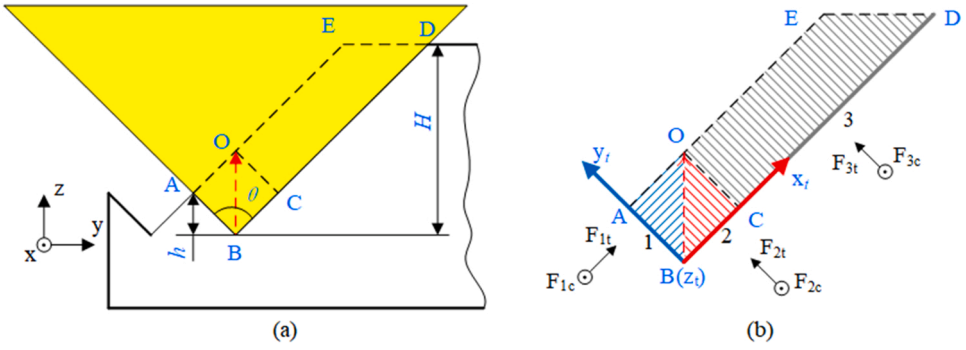

Fig. 3. Partition analysis of the (a) cutting area and (b) tool edge during non-free cutting.

segment. Due to the negligible influence on non-free cutting, the CD segment is approximated as the free-cutting tool edge. The rear side edge BA and the front side edge BC are symmetrical, and their chip removal directions are left-right symmetrical during cutting, causing chip removal interference. Therefore, the material with the quadrilateral cross-section ABCO is the primary non-free cutting area affecting the deformation of the micron-submicron grooves. The tool tip point B is the origin, and the BA tool edge is the y_t-axis. A local coordinate system (B-x_t-y_t-z_t) is established to describe the tool edge and the shear surface of the tool.

The rear side edge BA and the front side edge BC are separated and regarded as the free-cutting tool edges. However, they differ from the free-cutting tool edge used in the Merchant model. In the Merchant model, the tool edge is considered as a whole to quantify the shear angle and cutting force, and the shear stress is regarded as being independent of the shear angle. This approach is not suitable for non-free cutting. The degree of chip removal interference differs at different positions on BA and BC, resulting in different cutting microstates at the tool edges. Therefore, we introduce the concept of "infinitesimally segmenting tool edge" to assist the description of the local cutting microstate at different positions of the tool edges in non-free cutting. In the concept of the "infinitesimally segmenting tool edge", each single tool edge, e.g. BA or BC, is composed of an infinite number of tool edge infinitesimal segments (TEISs), and the length of each TEIS could theoretically close to 0. Consequently, a mathematical model is established to define the local shear angle and shear stress in these TEISs.

Fig. 4 shows the mechanism that non-free cutting makes shear angle of the shear zone smaller than that in free cutting, and the local shear angle varies for different TEISs. The material shearing and flow at the tool edges BA and BC in free cutting are shown in Fig. 4(a). The moving direction of the shear zone and the flow direction of the chips are perpendicular to the respective tool edges. In non-free cutting, the shear zones of the tool edges on both sides intersect, causing motion interference of the shear zone and chip removal interference. In this case, the material at the bottom of the shear zone is negligibly affected by the tool edge on the other side, whereas the material at the intersection of the shear zones of the tool edges on both sides is simultaneously affected by these two tool edges. Therefore, the top of the shear zone is moved in the symmetrical plane by the combined effect of the two tool edges. The schematic diagram of the shear zone interference in this area is shown in Fig. 4b. It should be noted that this interference changes the local shear angle. The shear zone at the TEIS M is shown in Fig. 4c. The flow at the top of the shear zone in the direction perpendicular to the tool edge is restricted, whereas the flow at the bottom of the shear zone is only slightly affected. Thus, the local shear zone at the TEIS M is transformed to a smaller shear angle. The shear zone transformation differs for different TEISs and depends on the distance from the intersection position of the shear zones to the TEIS. TEIS N is closer to tip B of the tool. Thus, the intersection of the shear zones is closer to TEIS N. Therefore, the interference degree is higher and the shear angle is smaller at TEIS N. The reduction in the shear angle is related to the width of the shear zone. In addition, when the nose angle of the tool is small, the shear interference between the two tool edges is more pronounced, resulting in a smaller shear angle. Therefore, the local shear angle at the TEIS on line BA is newly proposed in this paper and expressed by Eq. (1):

$$\varphi(y_t) = \arctan\left[a\left(1 - \frac{w}{y_t \tan(\frac{\theta}{2}) + b}\right)\right] \tag{1}$$

where w is the width of the shear zone as defined in the work of Li et al. (2011). a and b are constants. y_t is the distance from the TEIS to tool tip B, and θ is the tool nose angle. a and b can be obtained by finding the limits:

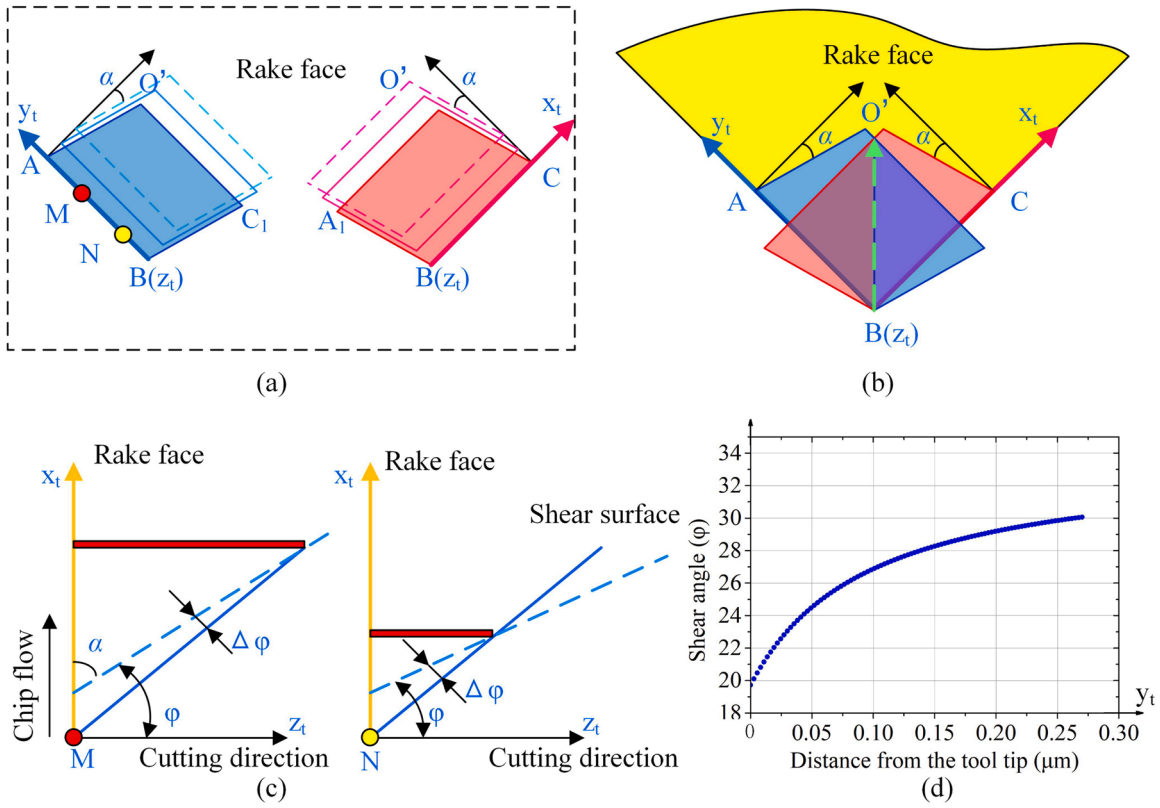

Fig. 4. Cutting microstate of the non-free cutting area. (a) Material shearing and flow at edges BA and BC in free cutting; α is the angle between the shear zone and the rake face. (b) The shear and chip removal interference between the tool edges on both sides; (c) principle of the variable shear angle due to shear and chip removal interference; φ is the angle of the shear zone, and Δφ is the difference in the local shear angle between non-free cutting and free cutting; (d) the trend of the local shear angle at the tool edge BA at tool nose angles of 90°.

$$\lim_{y_t \to +\infty} \varphi(y_t) = \arctan(a) = \frac{\pi}{4} - \frac{\beta}{2} \tag{2}$$

$$\lim_{y_t \to 0} \varphi(y_t) = \varphi_{crt} \tag{3}$$

When the distance from the TEIS to the tool tip is infinite, no interference occurs between the two tool edges, resulting in free cutting. Therefore, the value of a can be obtained by solving the limit, and the shear angle derived from Merchant's shear angle equation can be used as Eq. (2). When the TEIS is infinitely close to the tool tip, the interference is the largest; thus, the local shear angle reaches the minimum value φ_{crt}, as shown in Eq. (2). φ_{crt} cannot reach 0, otherwise, no chips are formed during cutting, resulting in anomalous cutting. Lee & Shaffer's shear angle equation regards the friction between the tool rake face and the chip as complete adhesive friction and does not consider the existence of sliding friction, so the calculated shear angle according to Lee & Shaffer's shear model is regarded as the limit value of the shear angle. The limit is calculated approximately equal to 20° when the rake angle γ_o and tangent of the friction angle between the chip and the tool are 0 and 0.4 respectively in this paper, so we set 20° for φ_{crt}. Fig. 4d shows the trend of the local shear angle at the tool edge BA at tool nose angles of 90°.

Based on the material's plastic incompressibility, the relationship between the velocity V_l of the material leaving the shear zone, the cutting speed V_c, and the shear angle can be expressed by Eq. (4), where the rake angle γ_o is 0. The tangent of φ is the ratio of the V_l and the V_c. Since φ at the TEIS is smaller at positions closer to the tool tip, V_l is also smaller, causing material accumulation, a temperature increase, and material sticking to the tool. It can explain the phenomenon of material accumulating and sticking to the tool tip area, which was found by Yan et al. (2009). Since additional material is removed as the cutting proceeds, the sheared material leaves the shear zone and eventually moves as a rigid body, forming chips. Fig. 5a and b show the shear surface of the front and rear tool edges as the shear angle changes in the local coordinate system B-x_t-y_t-z_t. Fig. 5c and d show the calculated morphology of the non-free shear surface at nose angles of 90°, based on the shear zone interference. The two sides of the non-free shear surfaces are symmetrical. The function of the intersecting curve of the two sides of y_t is expressed by Eq. (5). According to the expression of the shear surface and the middle intersection line, the opening of the local shear surface increases as the TEIS moves away from the tool tip. This result demonstrates that the shear surface meets the condition for chip formation and removal, and the proposed variable shear angle model is feasible.

$$V_l = V_c \frac{\sin\varphi}{\cos(\varphi - \gamma_o)} = V_c \tan\varphi, \varphi < 45^o$$

$$\tan\varphi = \frac{V_l}{V_c}, 0 < \tan\varphi < 1 \tag{4}$$

$$z_t(y_t) = \frac{{y_t}^2 + by_t}{a(y_t + b) - aw} \tag{5}$$

3. Mechanics model and deformation mechanism of micron-submicron groove cutting

The material suffers plastic deformation and strain hardening in the shear zone; therefore, as demonstrated by Astakhov et al. (2001), the shear zone is not an ideal surface but has a certain width. Therefore, the UDSZ theory is used to investigate the shear zone of the variable shear angle model. It is assumed that the width of the shear zone at all TEISs is w. Fig. 6(a) shows the non-free cutting removal model. The initial shear

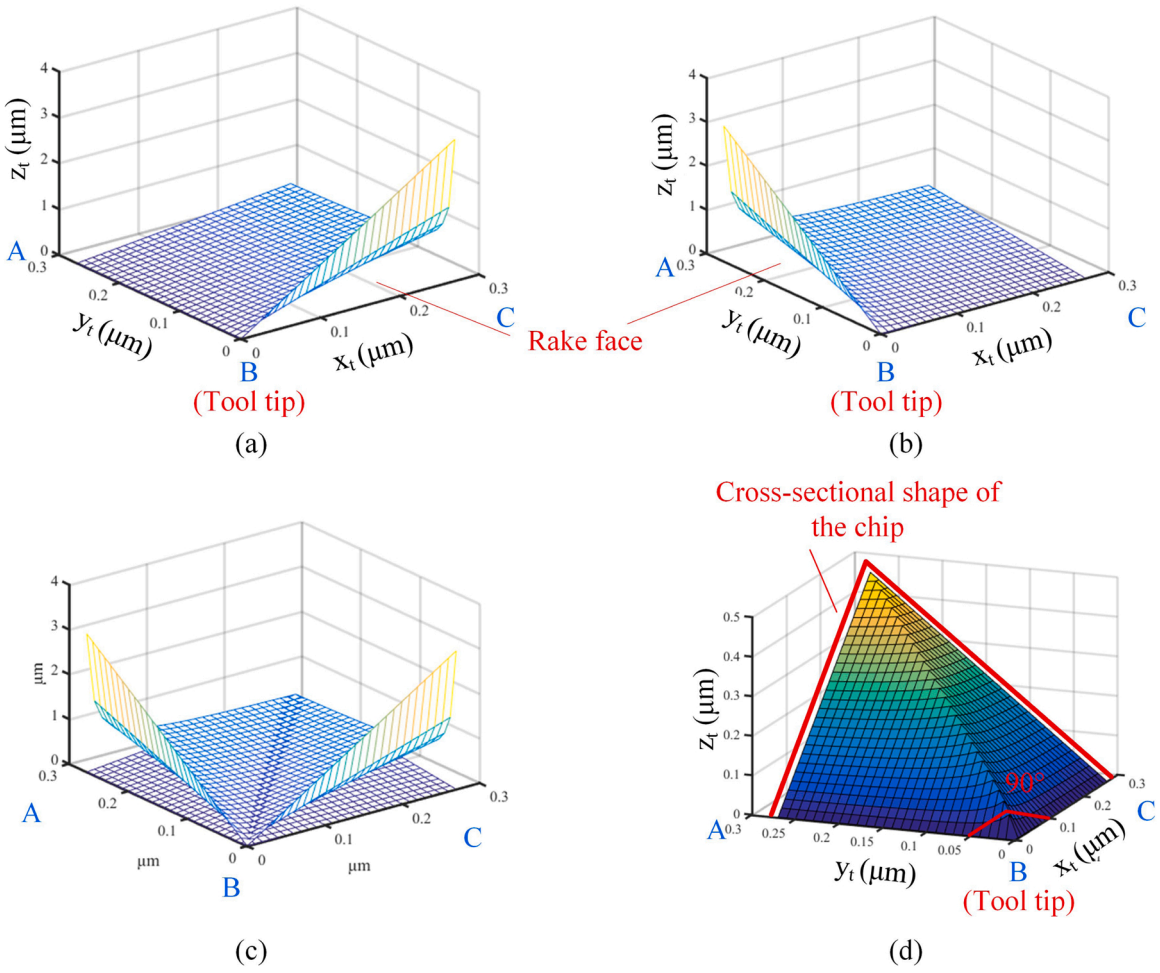

Fig. 5. The shape of the non-free shear surface in the local coordinate system B-x_t-y_t-z_t on the rake face. (a) The shear surface on the rear-edge BA, (b) the shear surface on the front-edge BC, (c) the resultant shear surface, and (d) the shape of the non-free shear surface between the two tool edges and the chip cross-section.

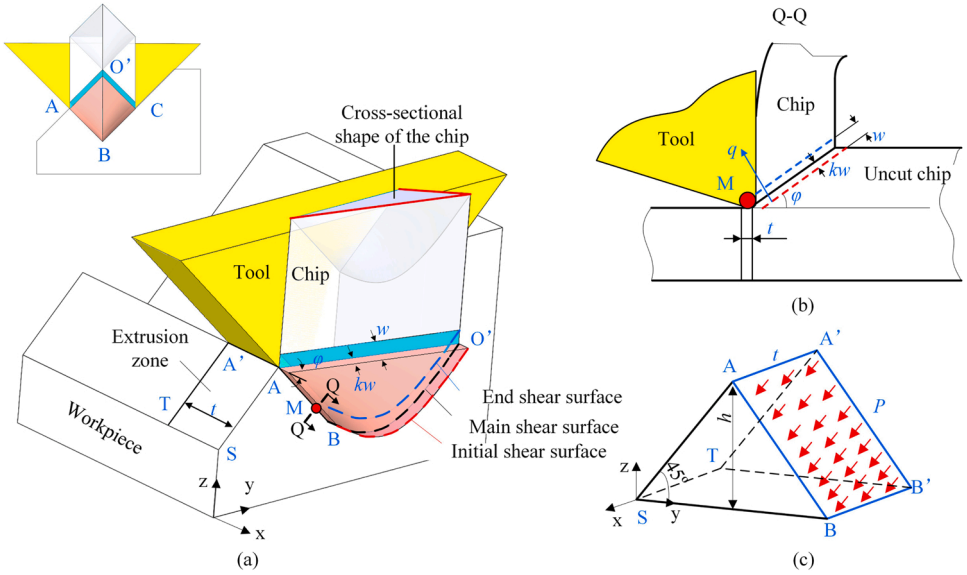

Fig. 6. (a) Schematic diagram of the variable shear angle removal model in the non-free cutting area, (b) UDSZ at TEIS M, and (c) the stress distribution on the surface of the micron-submicron groove.

surface, main shear surface, and end shear surface at all TEISs are combined. As mentioned above, they all are spatial surfaces. The shear zone at TEIS M is shown in Fig. 6b, where the drawing plane is perpendicular to the tool edge BA. The strain rate of the main shear surface is the highest, and it is assumed that the shear stress is uniformly distributed over the shear surface. The shear strain and shear strain rate of the main shear surface are obtained according to the velocity boundary conditions and compatibility conditions (Li et al., 2011).

$$\dot{\varepsilon}_m = 2V_c\cos(\gamma_0)/(w\cos(\varphi-\gamma_0)) \tag{6}$$

$$\varepsilon_m = \frac{k\cos\gamma_0}{\cos(\varphi-\gamma_0)\sin\varphi} \tag{7}$$

$$k = \cos(\varphi)\cos(\varphi-\gamma_0)/\cos(\gamma_0) \tag{8}$$

where $\dot{\varepsilon}_m$ and ε_m are the strain rate and strain of the main shear surface, k denotes the positional parameters of the main shear surface, V_c is the cutting velocity, γ_0 is the rake angle, and φ is the shear angle of the shear zone. The strain rate is assumed to change piecewise linearly, and the strain and strain rate in the shear zone can be expressed as:

$$\dot{\varepsilon} = \frac{q\dot{\varepsilon}_m}{kw}, q \in [0, kw] \tag{9}$$

$$\varepsilon = \frac{q^2\dot{\varepsilon}_m}{2kwV_c\sin\varphi}, q \in [0, kw] \tag{10}$$

where q denotes the coordinates of the shear surface in the shear zone.

The Johnson-Cook model describes the strain hardening and strain rate of materials during plastic deformation and is typically used to study processes with large strain rates. Moreover, the shear yield stress based on the von Mises criterion in the shear zone can be expressed as:

$$\tau = \frac{1}{\sqrt{3}}\left[A + B\left(\frac{\varepsilon}{\sqrt{3}}\right)^n\right]\left(1 + C\ln\frac{\dot{\varepsilon}}{\dot{\varepsilon}_0}\right)\left[1 - \left(\frac{T-T_r}{T_m-T_r}\right)^m\right] \tag{11}$$

where τ is the shear stress of the shear surface; A, B, C, n, and m are the material property constants. ε, $\dot{\varepsilon}$, and $\dot{\varepsilon}_0$ are the shear strain, shear strain rate, and reference strain rate, respectively. T, T_r, and T_m are the absolute temperatures of the shear surfaces, the reference temperature, and the melt temperature.

The third term in Eq. (11) is related to the conversion of plastic work into heat in the shear zone, and the thermal system in the shear zone can be regarded as adiabatic. The two-dimensional heat conduction of the shear zone is expressed in Eq. (12), where the temperature of the initial shear surface is equal to the initial temperature of the workpiece, which is the room temperature T_w. The boundary condition of the temperature is expressed as Eq. (13).

$$\frac{dT}{dq} = \mu\tau\dot{\varepsilon}\Big/(\rho c V_c\sin\varphi) \tag{12}$$

$$T|_{q=0} = T_w \tag{13}$$

where ρ, c, and μ are the material density, specific heat capacity, and Taylor-Quinney constant, respectively. According to the strain and strain rate in the shear zone, the first-order ordinary differential equation concerning the temperature (Eq. (10)) is numerically integrated to calculate the temperature in the shear zone and the temperature T_{mx} of the main shear surface.

The shear stress τ_m of the main shear surface is obtained by substituting Eqs. (6)–(8) and the temperature T_{mx} of the main shear surface into Eq. (11):

$$\tau_m = f(\varphi) \tag{14}$$

The shear stress on the main shear surface is related to the shear angle. The variable shear angle model shows that the shear angle differs at different TEISs; therefore, the shear stress is also different. We substitute Eq. (1) into Eq. (11) to calculate the shear stress.

According to Eq. (15), the cutting force $dF_{local\text{-}1}$ at a TEIS of BA consists of the main cutting force dF_{1c} and the thrust force dF_{1t}. The forces are related to the shear angle φ, the shear stress τ_m, the friction angle β between the tool and the chip, the TEIS length dy_t, and the local cutting thickness $\sqrt{2h}$ (using the tool nose angle of 90° as an example). The total cutting force $F_{local\text{-}1}$ of the edge BA can be obtained by Eq. (16). The extrusion stress σ acting on the groove surface by the tool edge can be expressed by Eq. (17). The edge radius is at least an order of magnitude smaller than the groove period; thus, its effect is ignored in this model. In real conditions, the contact width between the flank face and material is approximately equal along the tool edge BA, therefore, it is treated as a constant t, as shown in Fig. 6(a).

$$\overrightarrow{dF}_{local-1} = \begin{bmatrix} \&dF_{1c} \\ \&dF_{1t} \end{bmatrix} = \begin{bmatrix} \& \dfrac{\cos\beta}{\cos(\varphi+\beta)} \\ \& \dfrac{\sin\beta}{\cos(\varphi+\beta)} \end{bmatrix} \frac{\sqrt{2}\tau_m h dy_t}{\sin(\varphi)} \tag{15}$$

$$\overrightarrow{F}_{local-1} = \begin{bmatrix} \&F_{1c} \\ \&F_{1t} \end{bmatrix} = \begin{bmatrix} \& \displaystyle\int_A^B \frac{\cos\beta}{\cos(\varphi+\beta)} \frac{\sqrt{2}\tau_m h dy_t}{\sin(\varphi)} \\ \& \displaystyle\int_A^B \frac{\sin\beta}{\cos(\varphi+\beta)} \frac{\sqrt{2}\tau_m h dy_t}{\sin(\varphi)} \end{bmatrix} \tag{16}$$

$$\sigma = \frac{dF_{1t}}{t dy_t} = \frac{\sqrt{2}h\sin(\beta)}{t} \times \frac{\tau_m(\varphi)}{\cos(\varphi+\beta)\sin(\varphi)} \tag{17}$$

Since τ_m and φ differ for different TEISs, the extrusion stress σ also varies along the slope of the micron-submicron groove. After the cutting conditions have been determined, the first term in Eq. (17) is a constant, and the second term varies with the shear angle at the tool edge. The first and second derivatives of σ concerning y_t reflect the trend of the compressive stress on the slope.

$$\frac{d\sigma}{dy_t} < 0,$$

$$\frac{d^2\sigma}{dy_t^2} > 0 \tag{18}$$

According to Eq. (18), the extrusion stress increases sharply as y_t decreases. Therefore, the extrusion stress is higher on the slope area closer to the groove bottom, as shown in Fig. 6c.

Fig. 7a and b show the trends of τ_{mx} and σ at the tool edge BA at tool nose angles of 90°and the comparison with free-cutting at a nose angle of 180°. Non-free cutting causes the shear stress in the shear zone to increase sharply, increasing the extrusion stress on the micro-grooves. The bottom area of the groove suffers the highest extrusion stress due to the higher degree of non-free cutting. The extrusion stress at the bottom is near twice that of the top at a nose angle of 90°. The deformation of the micron-submicron grooves is also related to the local stiffness. Although the extrusion stress is smaller at the top of the groove, the material has a lower stiffness, resulting in higher deformation. The static mechanics model and computational analysis reveal the internal causes of cutting-induced deformation of the micron-submicron grooves. In real dynamic machining, the induced deformation results in material flow, a relative shift of the cutting line, and material residue.

4. Dynamic deformation of micron-submicron grooves based on FEM

4.1. Material settings and simulation methodology

The static mechanics model and computational analysis prove that the deformation characteristics of the micron-submicron grooves are

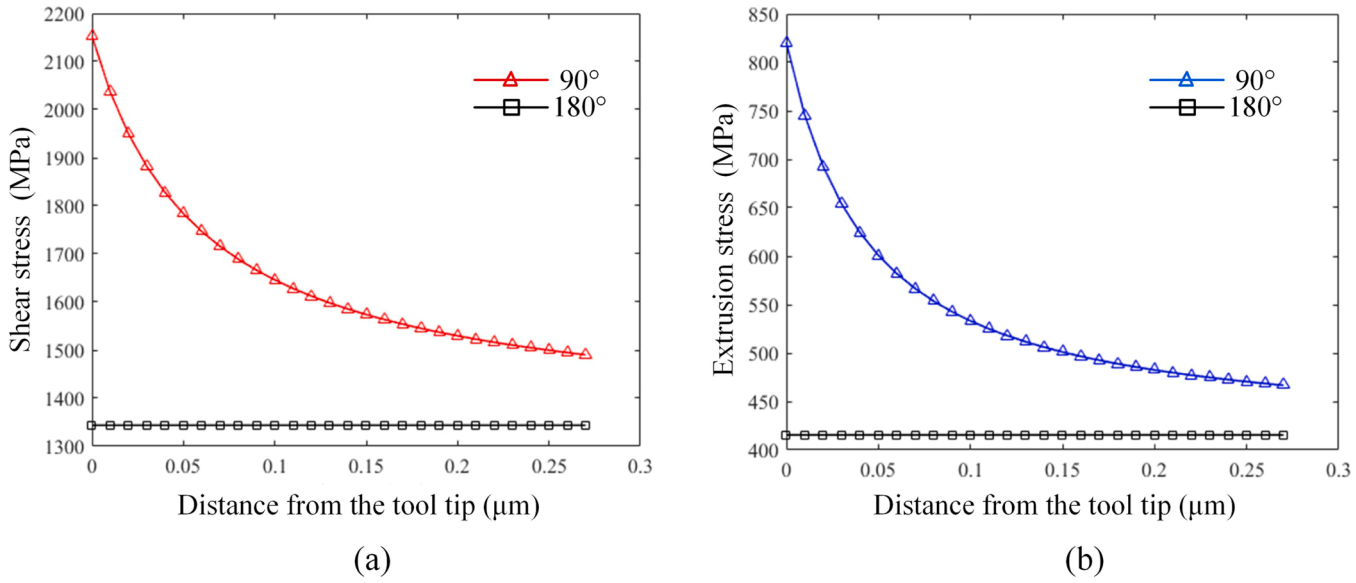

Fig. 7. The trends of (a) τ_{mx} of the main shear surface and (b) σ on the micron-submicron groove surface at the tool edge BA at nose angles of 90°.

related to the force distribution and the local stiffness. Since the induced deformation causes material flow and changes the cutting microstate between the tool and material, the final deformation and material residue after the dynamic deformation are investigated with the FEM. The Abaqus software supports the Johnson-Cook material constitutive model, which is consistent with the proposed mechanics model. In this FEM model, a groove is preset on the rear side of the current groove. The cutting speed is 9.4 μm/μs, and the material properties of the Ni-P and diamond tool are based on the test results and the data provided by the supplier, as shown in Table 1. The V-shaped tool has a nose angle of 90°, and the interaction type between the material and tool is "General contact (Explicit)", in which the friction coefficient set for the "Penalty" and fraction of converted heat distributed to workpiece are 0.4 and 0.5, respectively. The analysis step is typed with "Dynamic, Temp-disp, Explicit". The coupled temperature-displacement element named C3D8RT was utilized in this simulation, and the mesh size of the workpiece and tool are 10 nm and 20 nm, respectively. In the section of boundary condition setting, the bottom surface of the workpiece is totally fixed in six degrees of freedom.

Table 1
Material property settings of the Ni-P and diamond tools in the FEM.

Materials	Parameters	Value	Parameters	Value
Ni-P	Density (kt/m^3)	0.0082	Expansion (K^{-1})	1.3E-5
	Young's modulus (MPa)	1.62E5	Specific heat (J/(Kg·K))	460
	Poisson's ratio	0.25	Nonelastic heat fraction	0.9
	Conductivity (w/m·C)	5.02		
J-C model of Ni-P	A	400	d_3	-0.3
	B	1798	d_4	0.07
	n	0.9143	d_5	2.5
	C	0.0312	Melting temperature (K)	1533
	m	1.3	Transition temperature (K)	298
	d_1	0.239	Reference strain rate	1
	Displacement at failure	0.01	Epsilon dot zero	1
	d_2	0.456		
Diamond tool	Density (kt/m^3)	0.0032	Expansion (K^{-1})	4.7E-8
	Conductivity (w/m·C)	20.8	Specific heat (J/(Kg·K))	3115
	Young's modulus (MPa)	9.6E5		

The nodes on both sides of the tool edges are extracted to determine the differences in the degree of non-free cutting at different TEISs and verify the existence of variable shear angles during non-free cutting. Since differences in the degree of non-free cutting at different TEISs cannot be presented proportionally by the nodal stress at the tool edge due to the plastic property of the tool, only the elastic properties are used for the diamond tool. Therefore, the stress of the elastic nodes increases with the degree of non-free cutting. The elastic modulus of the diamond tool is very large, and the deformation is very small. Therefore, the elastic setting does not cause large errors in the deformation of the groove. The material flow during the dynamic deformation and the material residue after the dynamic deformation of the micron-submicron grooves are investigated, and the stress of the elastic nodes on the tool edges is also studied.

4.2. Dynamic deformation of micron-submicron grooves

As shown in Fig. 8a, monitoring nodes are used on the slope of the preset rear groove for calculating the degree of deformation. In the cutting simulation of grooves with a period of 380 nm, chip removal interference results in chip flow on the rake face parallel to the plane of symmetry. The chips are spread over the entire surface, as shown in Fig. 8b. The shear zone has a width of 100 nm. It should be mentioned that the nodes have a small failure displacement to prevent calculation errors caused by large deformation, the failure displacement value is set to be 0.1 μm. Therefore, meshed nodes in the middle of the chip are deleted after large deformation, making chip splitting happens in simulation, which may be not real in the experiment and just a necessary sacrifice to achieve the calculation. The rear material of the current groove is permanently plastically deformed due to the extrusion of the tool, as shown in Fig. 8c. A comparison of the position of the rear-side material before and after cutting is shown in Fig. 8d. Deformation and displacement of the groove occur, and severe deformation on the top area results in a large amount of material residue.

The position of the rear-side slope is simulated to investigate the deformation evolution of the groove for different parameters, as shown in Fig. 9. The results for DoC of 190 nm (D190-P380), 665 nm (D665-P380), and 2000 nm (D2000-P380) for grooves with a period of 380 nm are shown in Fig. 9a. In the case of D190-P380, there is no third tool edge

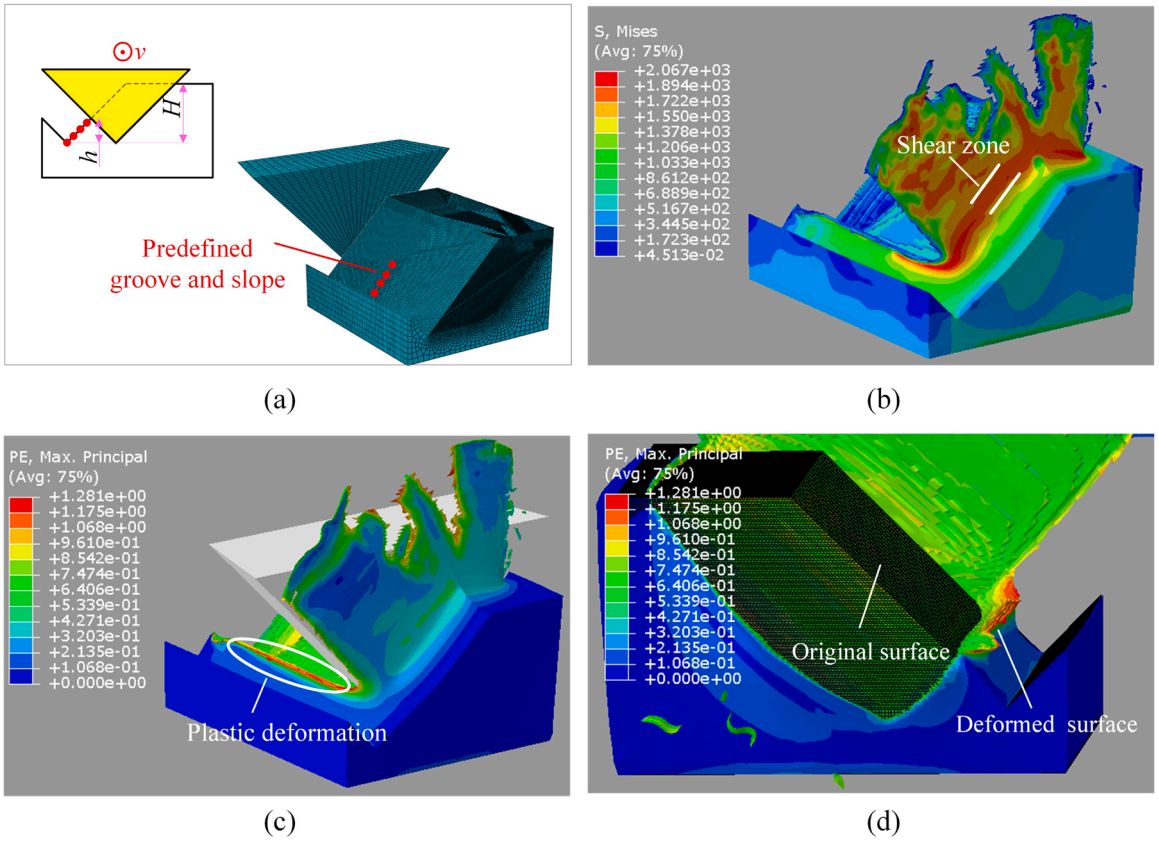

Fig. 8. 3D dynamic cutting simulation in Abaqus. (a) FEM model, (b) material removal and shear stress in the shear zone, (c) plastic deformation of the groove, and (d) position of the rear-side material before and after grooving.

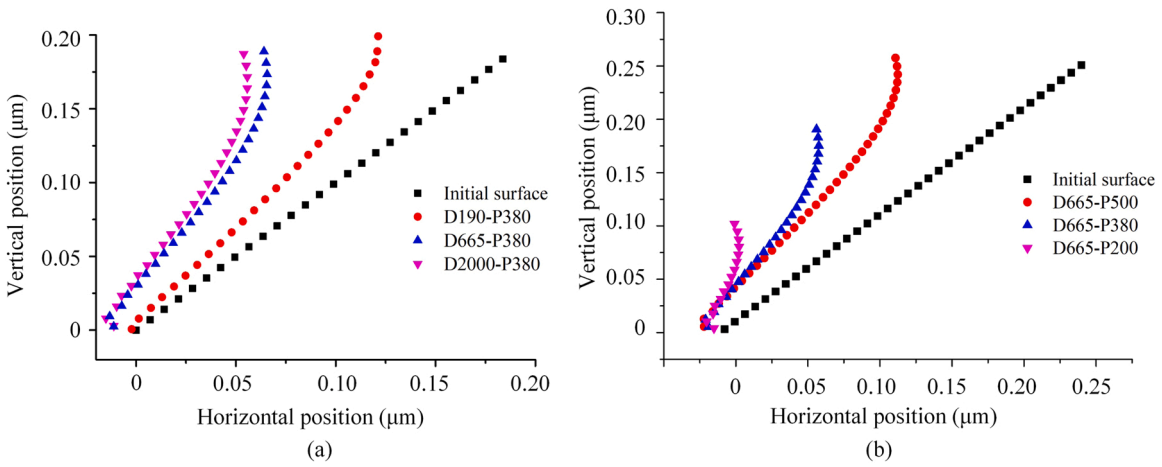

Fig. 9. The effects of the (a) depth of cut (DoC) and (b) the period on the deformation of the micron-submicron grooves.

CD, which was previously defined, and the contact lengths with the material are equal at the front and rear sides of the tool edges. The local cutting thickness decreases as the TEIS moves away from the tool tip, and D190-P380 simulates the ideal single-step machining of grooves. The bottom and top of the groove are deformed, and the lateral displacement of the top node exceeds 50 nm. It indicates that the deformation of the micron-submicron grooves occurs during non-free machining because of the chip removal interference. According to the illustration in Fig. 3a, when the DoC is larger than the twice of groove height (e.g., DoCs of 665 nm and 2000 nm), the local cutting thickness is the same at each TEIS. As shown in Fig. 9, for both D665-P380 and D2000-P380, the bottom material has a displacement of nearly 30 nm in the lateral direction, and the deformation of the top material increases by nearly 140 nm. The deformation of the groove depends on the local stiffness of the structure, and the deformation is smaller at the bottom than at the top due to the higher stiffness. As mentioned above, the deformation causes a forward shift in the relative cutting line of the rear side tool edge. The greater the deformation, the larger the shift is, causing more material residue to be moved to the rear. The deformation at the bottom of the groove is the same for D665-P380 and D2000-P380, and increasing the DoC only causes a small increase in the deformation of the top material. Therefore, it can be known that the deformation can not be reduced since the size of the non-free cutting area is the same when DoC is higher than the twice of groove height, which proves that

only considering the influence of the non-free cutting area on the submicron groove deformation has a high calculation accuracy. Consequently, decreasing the DoC to reduce the grooves deformation is only effective for DoC lower than the twice of groove height.

The stiffness of the micron-submicron groove is also proportional to the period. Fig. 9b shows the deformation results of grooves with periods of 200 nm (D665-P200), 380 nm (D665-P380), and 500 nm (D665-P500) with a DoC of 665 nm. The overall displacement of the bottom material is approximately equal for the grooves with these three periods, and the deformation and displacement of the top material always occur in the same length of the top area. The degree of deformation and the amount of residue of large grooves in the top area are relatively small compared to their size and can be regarded as burrs. However, in micron-submicron grooves, the degree of deformation and the amount of residue are equivalent to the groove size, resulting in a large angle change of the groove slope and low accuracy. This result demonstrates why the deformation caused by non-free cutting is typically ignored in large-scale groove machining but significantly affects the topographic accuracy in micron-submicron groove machining.

The von Mises stresses of the elastic nodes in the non-free cutting area on the front and rear sides of the tool edges were extracted. It should be noted that a diamond tool exhibits extremely high stress during cutting due to the large elastic modulus and elastic parameters. However, the stress distribution of the elastic nodes reflects the non-free cutting degree at different TEISs in equal proportions. This strategy can reveal the changes in the cutting microstate at the tool edge and the dynamic deformation of the micron-submicron grooves. Fig. 10 shows the stress of the elastic nodes on both sides of the tool edge during cutting for grooves with a period of 380 nm and different DoCs. The horizontal axis indicates the distance from the nodes to the tool tip. When the DoC is equal to the groove depth (D190-P380), the local cutting thickness decreases with an increase in the distance from the nodes to the tip increase, which makes the influence of the chip removal interference and stiffness difference between the front and rear materials on the edge stress not manifested. Therefore, the stress on both sides of the tool edges synchronously decreases. When the DoC is greater than the height of the groove (D650-P380), the local cutting thickness remains unchanged at the tool edge, indicating an influence of the chip removal interference and stiffness on the edge stress. As the distance from the tip increases, the nodal stress on the rear side of the tool edge decrease, and the degree of non-free cutting decreases. The nodal stress on the front side of the tool edge initially remains stable and increases slightly at the corresponding position, whereas the nodal stress on the rear side of the tool edge decreases rapidly. The drop in the nodal stress at the rear side of the tool edge is related to the top material's deformation, which causes more material to flow to the rear side. Therefore,

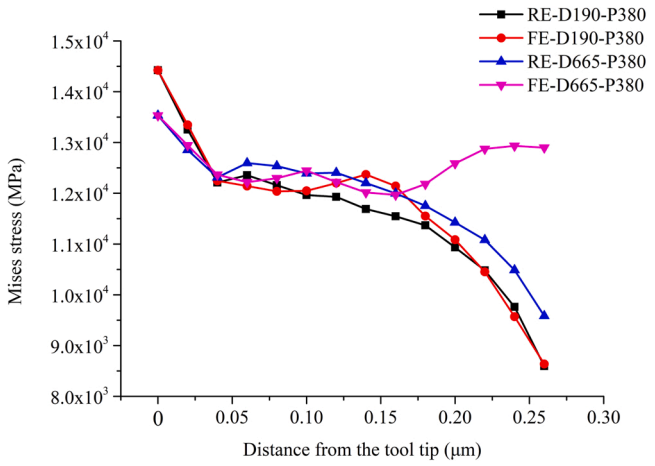

Fig. 10. The stress of the elastic nodes on both sides of the tool edge.

the local cutting thickness and the nodal stress increase at the front side of the tool edge. The nodal stress at the rear side of the tool edge verifies the proposed variable shear angle removal model and the mechanics model for micron-submicron groove non-free cutting. The degree of non-free cutting is higher at the TEIS closer to the tool tip.

5. Micron-submicron groove cutting experiment

5.1. Equipment setup and micron-submicron groove high-speed cutting

The micron-submicron groove cutting experiments are conducted on an ultra-precision machine (ULG-100, Toshiba, Japan), as shown in Fig. 11a. Since the cutting speed is very low (usually lower than 1 m/min) if only the translation servo axis is used, to reach a high cutting speed, the V-shaped tool is mounted perpendicularly with a large radius on the high-speed rotation axis and revolves. As shown in Fig. 11b, the rotation axis and tool turn in the axial direction (y-axis) to create micron-submicron grooves. Each groove is created by a single rotation of the tool; therefore, the groove period is controlled by matching the feed speed and rotation speed; and its accuracy depends on the motion accuracy of the machine. It should be noted, although the cutting path of the fly-cutting is a circular path unlike the straight cut illustrated in the above mode, the large radius of revolve makes the arc where the tool and workpiece interact with each other close to a straight line, and the grooves deformation investigated by characterizing the morphology of adjacent grooves with a same DoC is independent on this difference in this path. The rotation radius R is 30 mm, and the rotation speed is fixed at 3000 r/min. Thus, the cutting speed of the tool tip is 9.4 m/s, which is consistent with the simulation setting. Groove periods of 380 nm, 500 nm, 700 nm, and 1 μm are obtained by controlling the feed speed at 1.14 mm/min, 1.5 mm/min, 2.1 mm/min, and 3 mm/min, respectively. A V-shaped tool with a nose angle of 90° is symmetrically mounted which was achieved by fixing the tool on the designed tool holder, and so the angle of two sides of the tool edge with respect to the workpiece surface are both 45°. The deformation of the grooves with different periods is investigated.

5.2. V-shaped groove cutting and deformation analysis

The micron-submicron grooves are fabricated with the same DoC of 1120 nm using the tool with a nose angle of 90°, as shown in Fig. 12. It should be noted that the 1120 nm is measured value due to the tool setting error. The grooves in Fig. 12a–d have periods of 1000 nm, 700 nm, 500 nm, and 380 nm, respectively. The feed direction is from left to right, and the theoretical angle of all slopes is 45°. Based on the FEM results, the DoC of 1120 nm is larger than the twice of the height of all these grooves, so the biggest deformation happened to all these grooves. The grooves with a period of 1000 nm are tilted to the rear side after cutting, and the rear-side slope angle changes to around 90°. In addition, the material residue on the top of the grooves results in crooked ridges. At the same DoC, the grooves with a small groove period (700 nm/500 nm/380 nm) have a stronger tilt to the rear side because of the lower stiffness, and their rear-side slope angle changes more. In addition, the impact of the top material residue on the topographic accuracy of the grooves is larger. As shown in Fig. 12d, the residual material causes the groove ridge to become less straight.

The morphology of the grooves with a period of 380 nm was observed in detail. As shown in Fig. 13a, the top material residue results in a plateau on top of the groove with an average width of about 80 nm. The groove's cross-sectional profile in Fig. 13b was obtained from focused ion beam (FIB) microscopy, demonstrating that the bottom and top material of the groove have large deformations, and the groove is tilted to the rear. The deformation causes a 90° angle of the rear-side slope of the grooves. The top of the grooves is a small plateau instead of an ideal sharp point, indicating that the relative cutting line of the rear-side tool edge has shifted forward after deformation so that more

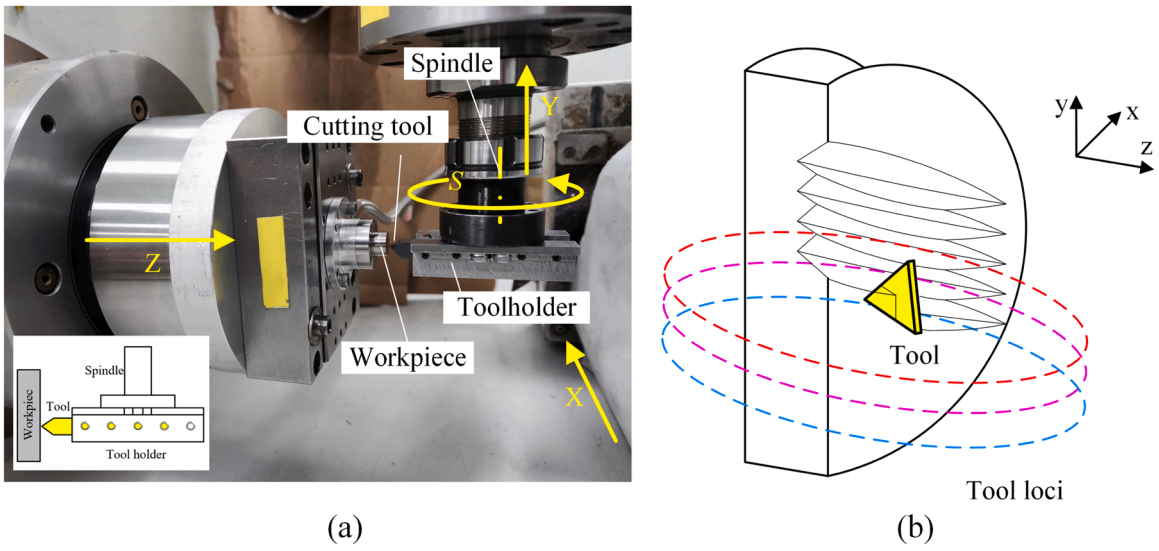

Fig. 11. (a) Experimental setup and (b) the high-speed micron-submicron groove cutting.

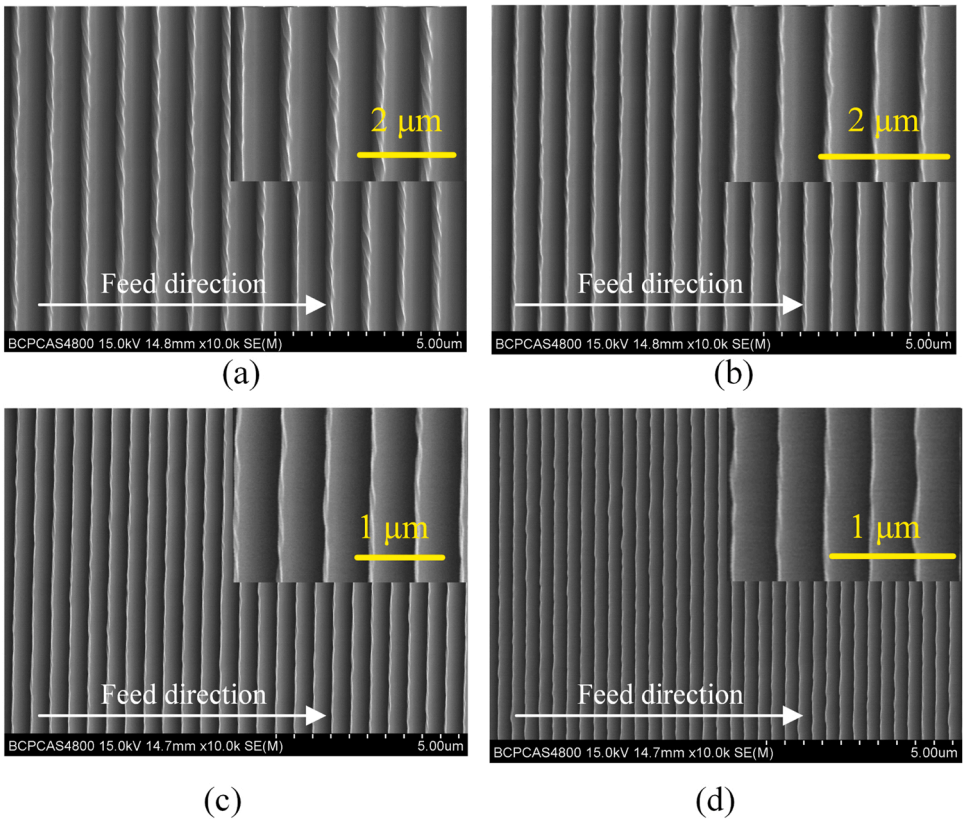

Fig. 12. Machined grooves with periods of (a) 1000 nm, (b) 700 nm, (c) 500 nm, and (d) 380 nm.

material is pushed to the rear side, forming a residue. Therefore, the dynamic deformation attributed to the structural stiffness changes the cutting microstate between the tool and material, which is a characteristic of the non-free cutting of micron-submicron grooves.

According to the FEM result shown in Fig. 9a, by decreasing the DoC to below the twice of the groove height, the size of the non-free cutting area could be further reduced with a decrease of the DoC, which can effectively reduce the cutting-caused deformation of the grooves. Therefore, a super small DoC of 240 nm was achieved and used in the grooves cutting by ensuring the tool setting error was below 150 nm. It should be noted that the 240 nm is a measured value since the actual DoC is not the set value due to the tool setting error. The cross-section profile of the machined grooves is shown in Fig. 14. It could be known that the deformation only happens in the top area of these grooves. The angle of the rear side slope of the groove has no obvious change, and the existing plateau formed due to the deformation of the top material of the grooves has a width of 70 nm. Compared with the result with a DoC of 1120 nm (Fig. 13b), the deformation of the grooves machined with the DoC of 240 nm is significantly reduced, verifying that the method to reduce the cutting-caused deformation by decreasing the DoC to below

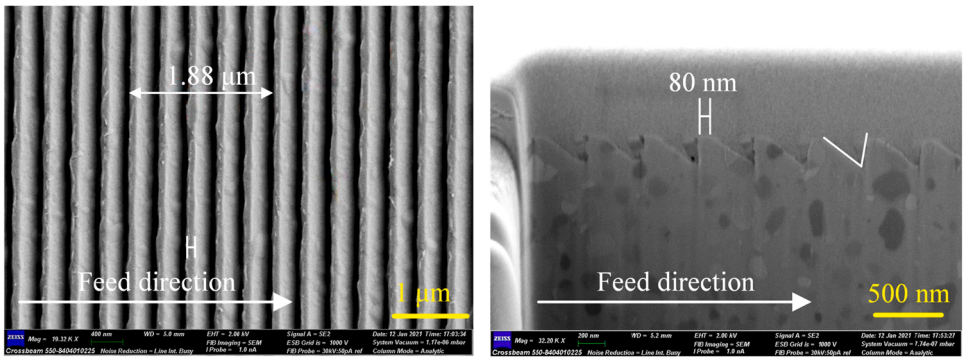

Fig. 13. Morphology of the machined grooves with a period of 380 nm. (a) top view of SEM image, (b) cross-sectional profile.

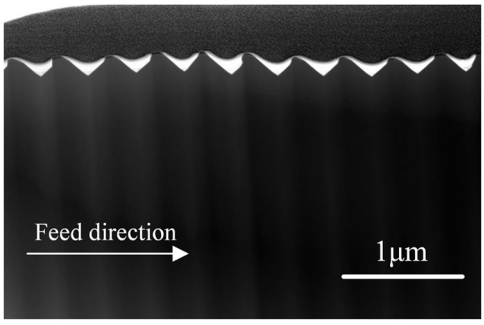

Fig. 14. The cross-sectional profile of the grooves with a period of 380 nm machined with DoC of 240 nm.

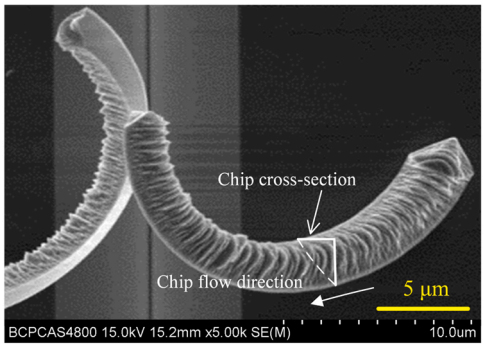

Fig. 15. Chip morphology of a single groove with a DoC of 5 μm.

the twice of groove height is effective.

In addition, the shear surface predicted by the proposed variable shear angle removal model is confirmed by the chip shape of the non-free cutting area. Fig. 15 shows the chip after cutting a single groove with a DoC of 5 μm, which is achieved by increasing the spacing between adjacent grooves to separate the grooves. Therefore, the material to be cut is all in a non-free cutting area, and the material shearing by both sides of the tool edge is symmetrical, resulting in a symmetrical cross-section of the chip. The chip topography reveals the shear and chip removal interference between the tool edges on both sides. The chip morphology is consistent with the experimental results obtained in the studies of Kobayashi et al. (2017) and Yan et al. (2009), and the cross-section conforms to the shape of the outermost boundary of the shear surface theoretically calculated in Section 2.2. The shear zone is formed during the cutting process, and the material accumulates and flows on the rake face to form a chip. As indicated in Fig. 5, the outer surface of the chip is the envelope of the outermost boundary of the shear surface on the flow path. The outermost boundary shown in Fig. 15 is approximately perpendicular to the chip flow direction, which is consistent with the results of the removal model in Section 2.2.

6. Conclusions

This paper provides new insight into the non-free cutting and cutting-induced deformation of micron-submicron grooves. The material shearing mechanism, chip evolution mechanism, and the deformation mechanism of the micron-submicron grooves during non-free cutting were revealed by establishing a novel removal model and a mechanics model. FEM simulations and cutting experiments were conducted to verify the cutting microstate of the tool edge and determine the dynamic deformation characteristics of the micron-submicron grooves, and the method to effectively reduce the cutting-caused deformation of grooves was finally determined.

The novel variable shear angle removal model, revealing the difference of material shear at different positions of the tool edge, is established by infinitesimally segmenting the tool edge after analyzing the shear interference and chip removal interference mechanisms. An equation of the local shear angle enables the mathematical derivation of the topography of the shear surface and chip cross-section in the non-free cutting of micron-submicron grooves. Since the degree of shear interference differed for different TEISs, the degree of local non-free cutting was higher for the TEIS closer to the tool tip, and the local shear angle was much smaller. The synthetic shear surface of the two tool edges is a 3D surface. The shear zone formed and moved continuously on the rake face, forming chips, and the outermost boundary of the shear surface determined the cross-section of the chip.

The mechanics model of micron-submicron groove cutting, revealing the deformation mechanism of the micron-submicron grooves, was established by developing the relationship between the shear angle and shear stress and using the differential cutting force method. The micron-submicron grooves were deformed by the extrusion of the rear-side tool edge, and the extrusion stress nearly doubled from top to bottom. The dynamic deformation characteristics of the micron-submicron grooves were related to the structural stiffness.

The mechanics model derived from the variable shear angle removal model was verified by the stress trend of the elastic nodes on the tool edge. The top of the groove had higher deformation than the bottom due to its lower stiffness. The deformation induced material flow, causing the relative cutting line of the rear-side tool edge to shift forward. Thus, a portion of the material was removed, and the remaining material was pushed back to form a residue. The results indicated that the non-free cutting area dominated the impact of micron-submicron groove cutting, therefore, reducing the size of the non-free cutting area by decreasing the DoC to below twice of the groove height is effective to

reduce the deformation of the groove. The deformation and displacement of the top material of grooves with different periods occurred in the same length of the top area.

The theoretical model and methods proposed in this paper will contribute to research on non-free cutting, chip formation, mechanical effects, and cutting-induced deformation of micron-submicron grooves.

CRediT authorship contribution statement

Yupeng He: Conceptualization, Methodology, Software, Writing – original draft. **Tianfeng Zhou:** Investigation, Data curation, Validation, Supervision. **A. Senthil Kumar:** Investigation, Writing – review & editing, Supervision. **Jiwang Yan:** Writing – review & editing, Supervision.

Declaration of Competing Interest

The authors declare that they have no known competing financial interests or personal relationships that could have appeared to influence the work reported in this paper.

Data availability

Data will be made available on request.

Acknowledgments

This work was financially supported by the National Natural Science Foundation of China (No. 51775046), the Beijing Municipal Natural Science Foundation (JQ20014), and the BIT Research and Innovation Promoting Project (2022YCXZ024).

References

Astakhov, V.P., Osman, M.O.M., Hayajneh, M.T., 2001. Re-evaluation of the basic mechanics of orthogonal metal cutting: velocity diagram, virtual work equation and upper-bound theorem. Int. J. Mach. Tools Manuf. 41, 393–418. https://doi.org/10.1016/S0890-6955(00)00084-5.

Dong, X., Zhou, T., Pang, S., Liang, Z., Yu, Q., Ruan, B., Wang, X., 2019. Comparison of fly cutting and transverse planing for micropyramid array machining on nickel phosphorus plating. Int. J. Adv. Manuf. Technol. https://doi.org/10.1007/s00170-019-03335-8.

Duong, T.H., Kim, H.C., 2015. Deformation analysis of rectangular channel structures in micro pattern machining. Int. J. Precis. Eng. Manuf. 16, 619–627. https://doi.org/10.1007/s12541-015-0083-4.

Duong, T.H., Kim, H.C., Lee, D.Y., Lee, S.W., Park, E.S., Je, T.J., 2013. A theoretical deformation prediction of micro channels in ultra-precision machining. Int. J. Precis. Eng. Manuf. 14, 173–181. https://doi.org/10.1007/s12541-013-0025-y.

Fang, F., Xu, F., 2018. Recent advances in micro/nano-cutting: effect of tool edge and material properties. Nanomanuf. Metrol. https://doi.org/10.1007/s41871-018-0005-z.

Fang, F., Zhang, N., Guo, D., Ehmann, K., Cheung, B., Liu, K., Yamamura, K., 2019. Towards atomic and close-to-atomic scale manufacturing. Int. J. Extrem. Manuf. https://doi.org/10.1088/2631-7990/ab0dfc.

Geng, Y., Yan, Y., Wang, J., Brousseau, E., Sun, Yanwen, Sun, Yazhou, 2018. Fabrication of periodic nanostructures using AFM Tip-based nanomachining: combining groove and material pile-up topographies. Engineering 4, 787–795. https://doi.org/10.1016/j.eng.2018.09.010.

He, Y., Zhou, T., Dong, X., Liu, P., Zhao, W., Wang, X., Hu, Y., Yan, J., 2020. Generation of high-saturation two-level iridescent structures by vibration-assisted fly cutting. Mater. Des. 193, 108839 https://doi.org/10.1016/j.matdes.2020.108839.

He, Y., Zhou, T., Dong, X., Zhu, Z., Yu, Q., Liu, P., Zhao, W., Wang, X., Hu, Y., Yan, J., 2021. Diffraction manipulation of visible light with submicron structures for structural coloration fabrication. Opt. Express 29, 9294. https://doi.org/10.1364/oe.419291.

Jiang, S., Hu, Y., Wu, H., Zhang, Yachao, Zhang, Yiyuan, Wang, Y., Zhang, Yinghui, Zhu, W., Li, J., Wu, D., Chu, J., 2019. Multifunctional Janus microplates arrays actuated by magnetic fields for water/light switches and bio-inspired assimilatory coloration. Adv. Mater. 31, 1–8. https://doi.org/10.1002/adma.201807507.

Kobayashi, R., Xu, S., Shimada, K., Mizutani, M., Kuriyagawa, T., 2017. Defining the effects of cutting parameters on burr formation and minimization in ultra-precision grooving of amorphous alloy. Precis. Eng. https://doi.org/10.1016/j.precisioneng.2017.01.018.

Kowalik, A., Góra, K., Jaroszewicz, Z., Kołodziejczyk, A., 2005. Multi-step electron beam technology for the fabrication of high performance diffractive optical elements. Microelectron. Eng. 77, 347–357. https://doi.org/10.1016/j.mee.2004.12.036.

Li, B., Wang, X., Hu, Y., Li, C., 2011. Analytical prediction of cutting forces in orthogonal cutting using unequal division shear-zone model. Int. J. Adv. Manuf. Technol. 54, 431–443. https://doi.org/10.1007/s00170-010-2940-8.

Li, G., Xu, Z., Fang, F., Wu, W., Xing, X., Li, W., Liu, H., 2013. Micro cutting of V-shaped cylindrical grating template for roller nano-imprint. J. Mater. Process. Technol. 213, 895–904. https://doi.org/10.1016/j.jmatprotec.2012.12.010.

Malshe, A., Rajurkar, K., Samant, A., Hansen, H.N., Bapat, S., Jiang, W., 2013. Bio-inspired functional surfaces for advanced applications. CIRP Ann. Manuf. Technol. https://doi.org/10.1016/j.cirp.2013.05.008.

Qiao, W., Huang, W., Liu, Y., Li, X., Chen, L., Sen, Tang, J.X., 2016. Toward scalable flexible nanomanufacturing for photonic structures and devices. Adv. Mater. 28, 10353–10380. https://doi.org/10.1002/adma.201601801.

Qiao, Z., Qu, D., Wang, H., Wu, D., Wang, B., 2018. Experimental investigation of the influence of chip interference on burr height in machining micro V-grooves on electroplated copper roll die. Proc. Inst. Mech. Eng. Part B J. Eng. Manuf. 232, 1491–1497. https://doi.org/10.1177/0954405416668927.

Shi, H., 2018. The Chip-Ejection Interference and Compromise in Non-free Cutting. In: Metal Cutting Theory. Springer Series in Advanced Manufacturing. Springer, Cham. https://doi.org/10.1007/978-3-319-73561-0_7.

Shi, H.M., Wang, J.L., 1995. A model for non-free-cutting. Int. J. Mach. Tools Manuf. 35, 1507–1522. https://doi.org/10.1016/0890-6955(95)00007-K.

Song, K.H., Choi, Y.J., Lee, Y.S., 2019. A study on the deformation behavior of a microstructure depending on its shape and the cutting section in the precision cutting of a functional part. Appl. Sci. 9. https://doi.org/10.3390/app9142940.

Sun, Z., To, S., Yu, K.M., 2018. One-step generation of hybrid micro-optics with high-frequency diffractive structures on infrared materials by ultra-precision side milling. Opt. Express 26, 28161. https://doi.org/10.1364/oe.26.028161.

Tauhiduzzaman, M., Yip, A., Veldhuis, S.C., 2015. Form error in diamond turning. Precis. Eng. 42, 22–36. https://doi.org/10.1016/j.precisioneng.2015.03.006.

Xue, B., Yang, C., Geng, Y., Yan, Y., 2021. A novel fabrication of micro/nano hierarchical grating structures for structural coloration by using revolving tip-based machining method. J. Manuf. Process. 62, 202–212. https://doi.org/10.1016/j.jmapro.2020.12.016.

Yan, J., Oowada, T., Zhou, T., Kuriyagawa, T., 2009. Precision machining of microstructures on electroless-plated NiP surface for molding glass components. J. Mater. Process. Technol. 209, 4802–4808. https://doi.org/10.1016/j.jmatprotec.2008.12.008.

Yan, Y., Geng, Y., Hu, Z., 2015. Recent advances in AFM tip-based nanomechanical machining. Int. J. Mach. Tools Manuf. 99, 1–18. https://doi.org/10.1016/j.ijmachtools.2015.09.004.

Yew Jin, N.T., Lim, Z.H., Zhou, G., Liu, K., Senthil Kumar, A., 2021. Design and fabrication of composite polygonal Fresnel lenses. Opt. Express 29, 36516. https://doi.org/10.1364/oe.436290.

Zhang, X., Sui, H., Zhang, D., Jiang, X., 2018. An analytical transient cutting force model of high-speed ultrasonic vibration cutting. Int. J. Adv. Manuf. Technol. 95, 3929–3941. https://doi.org/10.1007/s00170-017-1499-z.

Zhou, F., Hua, J., Shi, J., Qiao, W., Chen, L., 2020. Pixelated blazed gratings for high brightness multiview holographic 3D display. IEEE Photonics Technol. Lett. 32, 283–286. https://doi.org/10.1109/LPT.2020.2971147.

Zhu, L., Li, Z., Fang, F., Huang, S., Zhang, X., 2018a. Review on fast tool servo machining of optical freeform surfaces. Int. J. Adv. Manuf. Technol. https://doi.org/10.1007/s00170-017-1271-4.

Zhu, W. Le, Duan, F., Zhang, X., Zhu, Z., Ju, B.F., 2018b. A new diamond machining approach for extendable fabrication of micro-freeform lens array. Int. J. Mach. Tools Manuf. 124, 134–148. https://doi.org/10.1016/j.ijmachtools.2017.10.007.

Zhu, Z., To, S., Zhang, S., 2015. Theoretical and experimental investigation on the novel end-fly-cutting-servo diamond machining of hierarchical micro-nanostructures. Int. J. Mach. Tools Manuf. 94, 15–25. https://doi.org/10.1016/j.ijmachtools.2015.04.002.